Raman tensor of AlN bulk single crystal

Wei Zheng,[1] Ruisheng Zheng,[2,4] Feng Huang,[1,*] Honglei Wu,[2] and Fadi Li[3]

[1]*State Key Laboratory of Optoelectronic Materials and Technologies, School of Physics and Engineering, Sun Yat-Sen University, Guangzhou 510275, China*
[2]*Institute of Optoelectronics, Shenzhen University, Shenzhen 518060, China*
[3]*Institute of Solid State Physics, Chinese Academy of Sciences, Hefei 230031, China*
[4]*e-mail: rszheng@szu.edu.cn*
**Corresponding author: huangfeng@mail.sysu.edu.cn*

Received October 28, 2014; revised December 17, 2014; accepted December 17, 2014; posted January 7, 2015 (Doc. ID 225675); published March 17, 2015

The angle dependence of optical phonon modes of an AlN bulk single crystal from the *m*-plane (1$\bar{1}$00) and *c*-plane (0001) surfaces, respectively, is investigated by polarized Raman spectroscopy in a backscattering configuration at room temperature. Corresponding Raman selection rules are derived according to measured scattering geometries to illustrate the angle dependence. The angle-dependent intensities of phonon modes are discussed and compared to theoretical scattering intensities, yielding the Raman tensor elements of A_1(TO), E_2^2, E_1(TO), and A_1(LO) phonon modes and the relative phase difference between the two complex elements of A_1(TO). Furthermore, the Raman tensor of wurtzite AlN is compared with that of wurtzite ZnO reported in previous work, revealing the intrinsic differences of lattice vibration dynamics between AlN and ZnO. © 2015 Chinese Laser Press

OCIS codes: (160.6000) Semiconductor materials; (290.5860) Scattering, Raman; (290.5855) Scattering, polarization.
http://dx.doi.org/10.1364/PRJ.3.000038

1. INTRODUCTION

AlN is a promising semiconductor for vacuum- and deep-ultraviolet application [1–3], due to its remarkable physical properties, including an ultrawide band gap of 6.2 eV, superior radiation resistance, high chemical and thermal stability, and high melting temperature [4,5]. Investigating the vibration properties of phonons in AlN is very important for AlN-based devices, because AlN is a polar semiconductor, which will cause substantial joule heating under high current densities [6,7], mainly resulting from the Fröhlich electron–phonon interaction [8]. Raman spectroscopy is a powerful technique to probe the vibrational mode behavior of materials, providing information about the symmetry of the vibrational mode, the crystal structure and quality, and the lattice defect. The earliest study on Raman spectra of wurtzite AlN was published in the 1960s and determined the fundamental vibrational modes of AlN crystals [9]. Since then, Raman spectra of AlN have been studied intensively [10–19]. However, some problems remain unsolved, such as the determination of the Raman tensor.

In this work, we present the angle-dependent polarized Raman spectra by parameterizing the incoming and scattered polarization vectors from a hexagonal AlN bulk single crystal and compare them with calculated Raman intensities extracted from Raman selection rules. Such a process gives a full mode assignment and determines the Raman tensor elements of wurtzite AlN. Moreover, the differences between the Raman tensor of wurtzite AlN and that of ZnO are particularized and discussed in detail.

Typically, AlN and ZnO single crystals both have wurtzite symmetry, which belongs to the space group C_{6v}^4 ($P6_3mc$). The differences between AlN and ZnO in spontaneous polarization, piezoelectric constants [20], radiation anisotropy [21–24], etc., lead them to different applications in the field of optoelectronics. This work provides new insight into the intrinsic difference of lattice vibration dynamics between AlN and ZnO materials.

2. EXPERIMENTAL DETAILS

A hexagonal prismatic AlN bulk single crystal (see inset in Fig. 1) was grown by the physical vapor transport (PVT) method at 2150°C in a nitrogen environment using a tungsten crucible [25]. The crystal structure was analyzed by high-resolution x-ray diffractometry (HR-XRD) (Rigaku, TTRAX III, Cu Kα, 18 W). All diffraction peaks can be indexed to a relaxed wurtzite-type AlN structure. Micro-Raman measurements were carried out via a Renishaw Raman spectrometer (inVia Reflex) with spectral resolution of 1.5 cm^{-1}, using a 532 nm laser (Samba CW DPSS) with a power of 3 mW for exciting light. The 532 nm laser was focused on the *m*- and *c*-plane surfaces of the AlN crystal, respectively, via a 50× objective. Raman scattered light was collected in backscattering geometry, and was then dispersed by a spectrometer with a 250 mm focal length, and finely detected by a CCD detector.

To enable the measurement part of the scattered light with polarization parallel (or perpendicular) to that of incoming light, a rotatable polarizer was inserted in the scattering light path. A microscope stage rotated around the axis along the direction of the incoming laser was used to observe angle-dependent Raman spectra. The configuration of our experiment is presented in Fig. 1. *xyz* is congruous with the crystal axes of AlN crystal where the *z* axis is parallel to the *c* axis. As

 © 2015 Chinese Laser Press

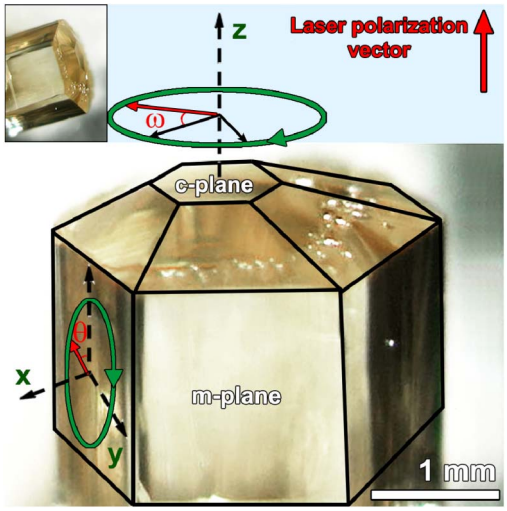

Fig. 1. Schematic illustration of AlN single crystal and Raman scattering coordinate system. The c-plane and m-plane of AlN single crystal are easy to identify. The c-plane is perpendicular to the z axis (i.e., c axis), while the m-plane is perpendicular to the x axis (i.e., a axis). The red arrows denote the polarization vectors of the incident laser. The AlN sample can be rotated around the z axis (x axis) when the wave vector of the incoming laser is along the z axis (x axis), where ω (θ) is the rotation angle with respect to the x axis (z axis).

incident light is set along the z axis, the AlN sample can be rotated around the z axis, and the rotation angle ω is between the polarization vector of incident light and the x axis; as incident light is set along the x axis, the AlN sample can be rotated around the x axis and the rotation angle θ is between the polarization vector of incident light and the z axis.

3. RAMAN SELECTION RULES

In a wurtzite AlN crystal structure in which a per primitive unit cell contains four atoms, there are nine optical phonon modes that reduce to 1 A_1, 2 B_1, 1E_1, and 2 E_2 modes at the center of the Brillouin zone. According to group theory, both A_1 and E_1 modes are Raman- and infrared-active, where A_1 is polarized along the z direction, while E_1 is polarized in the xy plane. Due to bond polarity, Raman phonons with A_1 and E_1 symmetry exhibit frequency shifts. The E_2 mode, being twofold degenerate, is only Raman-active. The two B_1 modes are silent modes [26].

For the Raman-active optical phonon modes, the intensity $\boldsymbol{I}$ of Raman scattering is given by [27,28]

$$I \sim |\boldsymbol{e}_s \cdot \boldsymbol{R} \cdot \boldsymbol{e}_i|^2, \tag{1}$$

where $\boldsymbol{e}_i$ and $\boldsymbol{e}_s$ represent the unit polarization vectors of incident and scattered light, respectively. $\boldsymbol{R}$ is the complex second-rank Raman tensor [29], which is represented by a complex 3×3 matrix. This matrix describes the properties of a phonon mode with respect to Raman scattering. The Raman tensor of Raman-active A_1, E_1, and E_2 modes in a wurtzite material is given by [27,28]

$$\boldsymbol{R}[A_1] = \begin{bmatrix} a & 0 & 0 \\ 0 & a & 0 \\ 0 & 0 & b \end{bmatrix} = \begin{bmatrix} |a|e^{i\varphi_a} & 0 & 0 \\ 0 & |a|e^{i\varphi_a} & 0 \\ 0 & 0 & |b|e^{i\varphi_b} \end{bmatrix}, \tag{2}$$

$$\boldsymbol{R}[E_1] = \begin{bmatrix} 0 & 0 & -c \\ 0 & 0 & c \\ -c & c & 0 \end{bmatrix} = \begin{bmatrix} 0 & 0 & -|c|e^{i\varphi_c} \\ 0 & 0 & |c|e^{i\varphi_c} \\ -|c|e^{i\varphi_c} & |c|e^{i\varphi_c} & 0 \end{bmatrix}, \tag{3}$$

$$\boldsymbol{R}[E_2] = \begin{bmatrix} d & d & 0 \\ d & -d & 0 \\ 0 & 0 & 0 \end{bmatrix} = \begin{bmatrix} |d|e^{i\varphi_d} & |d|e^{i\varphi_d} & 0 \\ |d|e^{i\varphi_d} & -|d|e^{i\varphi_d} & 0 \\ 0 & 0 & 0 \end{bmatrix}, \tag{4}$$

where a, b, c, and d denote the Raman tensor elements, and φ_a, φ_c, φ_d, and φ_b denote the complex phase of the Raman tensor elements. For Raman backscattering measurements on the m-plane surface, the polarization vectors of incident and scattering light referred to the hexagonal axes can be written as

$$\boldsymbol{e}_i = \begin{pmatrix} 0 \\ \sin(\theta) \\ \cos(\theta) \end{pmatrix} \quad \text{and} \quad \boldsymbol{e}_s = \begin{pmatrix} 0 \\ \sin(\theta_s) \\ \cos(\theta_s) \end{pmatrix}, \tag{5}$$

where θ (θ_s) represents the angle between the z axis of the sample and the polarization vector of the incident (scattered) light. For Raman backscattering measurements on the c-plane surface, the polarization vectors of incident and scattering light referred to the hexagonal axes can be written as

$$\boldsymbol{e}_i = \begin{pmatrix} \cos(\omega) \\ \sin(\omega) \\ 0 \end{pmatrix} \quad \text{and} \quad \boldsymbol{e}_s = \begin{pmatrix} \cos(\omega_s) \\ \sin(\omega_s) \\ 0 \end{pmatrix}, \tag{6}$$

where $\omega(\omega_s)$ represents the angle between the x axis of the sample and the polarization vector of the incident (scattered) light.

Here, we have discussed the parallel ($\boldsymbol{e}_i \| \boldsymbol{e}_s$, e.g., $\theta_s = \theta$ or $\omega_s = \omega$) and perpendicular ($\boldsymbol{e}_i \perp \boldsymbol{e}_s$, e.g., $\theta_s = \theta + \pi/2$, $\omega_s = \omega + \pi/2$) scattering configurations. For these configurations, according to Eq. (1), the Raman intensity can be expressed in the following cases.

A. Raman Backscattering Measurements on *m*-Plane Surface

For $\boldsymbol{e}_i \| \boldsymbol{e}_s$ scattering configurations,

$$I^{\|}_{A_1}(\theta) \sim |a|^2 \sin^4\theta + |b|^2 \cos^4\theta + \frac{1}{2}|a||b| \sin^2(2\theta)\cos(\varphi_{a-b}), \tag{7}$$

$$I^{\|}_{E_1}(\theta) \sim \frac{|c|^2}{2}\sin^2(2\theta), \tag{8}$$

$$I^{\|}_{E_2}(\theta) \sim |d|^2 \cos^4\theta \tag{9}$$

with $\varphi_{a-b} = \varphi_a - \varphi_b$.

For $\boldsymbol{e}_i \perp \boldsymbol{e}_s$ scattering configurations,

$$I^{\perp}_{A_1}(\theta) \sim \frac{1}{4}[|a|^2 + |b|^2 - 2|a||b|\cos(\varphi_{a-b})]\sin^2(2\theta), \tag{10}$$

$$I^{\perp}_{E_1}(\theta) \sim |c|^2 \cos^2(2\theta), \tag{11}$$

$$I_{E_2}^{\perp}(\theta) \sim \frac{|d|^2}{4}\sin^2(2\theta). \tag{12}$$

B. Raman Backscattering Measurements on *c*-Plane Surface

For $\boldsymbol{e_i}\|\boldsymbol{e_s}$ scattering configurations,

$$I_{A_1}^{\|}(\theta) \sim |a|^2, \tag{13}$$

$$I_{E_1}^{\|}(\theta) \sim 0, \tag{14}$$

$$I_{E_2}^{\|}(\theta) \sim |d|^2. \tag{15}$$

For $\boldsymbol{e_i}\perp\boldsymbol{e_s}$ scattering configurations,

$$I_{A_1}^{\perp}(\theta) \sim 0, \tag{16}$$

$$I_{E_1}^{\perp}(\theta) \sim 0, \tag{17}$$

$$I_{E_2}^{\perp}(\theta) \sim |d|^2. \tag{18}$$

It should be noted that the phase difference φ_{a-b} between the Raman tensor elements a and b has a significant influence on the Raman scattering intensities of the A_1 mode. Figure 2 displays $I_{A_1}^{\|}(\theta)$ for one particular choice of values $|a|$ and $|c|$ and several different phase angles φ_{a-b}. It shows that the function $I_{A_1}^{\|}(\theta)$ is unique for any particular value of $|a|$, $|b|$, and φ_{a-b} and allows an unambiguous value of these three parameters, for instance, when the value of $I_{A_1}^{\|}(\theta)$ at $\theta = 0°$ and 90° is given by $|a|$ and $|b|$, respectively. This is not true for $I_{A_1}^{\perp}(\theta)$, by which different choices of $|a|$, $|b|$, and φ_{a-b} may produce identical line shapes. Nevertheless, $I_{A_1}^{\perp}(\theta)$ is still useful to check the parameters obtained from a determination of $I_{A_1}^{\|}(\theta)$.

4. RESULTS AND DISCUSSION

A. Angle-Dependent Polarized Raman Spectra of AlN

In Fig. 3(a), the Raman spectra from the *m*-plane surface of the AlN sample in a range of 560–720 cm^{-1} are shown for different rotation angles θ increasing from 0° to 180° with a step of 5° for parallel polarization vectors of the incoming laser and the scattered light $[x(zz)\underline{x} \rightarrow x(yy)\underline{x} \rightarrow x(zz)\underline{x}]$. For clarity, the spectra are shifted on both the x and y axes by a constant amount. The three modes with FWHM less than 4 cm^{-1} located at around 611, 657, and 671 cm^{-1} are ascribed to the allowed Raman-active phonon modes $A_1(TO)$, E_2^2 (e.g., E_2^{high}), and $E_1(TO)$, respectively. Between 0° and 180°, the $A_1(TO)$ mode never disappears completely and has a single intensity maximum at $\theta = 90°$ and two minima at 25° and 160° [see Fig. 4(a)]. The situation of the $E_1(TO)$ and E_2^2 mode is rather different from that of the $A_1(TO)$ mode. The $E_1(TO)$ mode has two maxima at $\theta = 45°$ and 135°, and three minima at $\theta = 0°, 90°$, and 180° [see Fig. 4(c)], whereas the E_2^2 mode has two maxima at $\theta = 0°$ and 180° and only one minimum at $\theta = 90°$. The Raman spectra from the *m*-plane surface for perpendicular polarization vectors of the incoming laser and the scattered light $[x(zy)\underline{x} \rightarrow x(yz)\underline{x} \rightarrow x(zy)\underline{x}]$ are shown in Fig. 3(b). Angle dependences of $A_1(TO)$, $E_1(TO)$, and E_2^2 are all in accordance with sinusoidal functions [see Figs. 4(b), 4(d), and 4(f)]. Both $A_1(TO)$ and E_2^2 have two intensity maxima at $\theta = 45°$ and 135°, and three minima at $\theta = 0°$, 90°, and 180°, while $E_1(TO)$ has three maxima at $\theta = 0°$, 90°, and 180°, and three minima at $\theta = 45°$ and 135°. Compared to the $E_1(TO)$ phonon, the $A_1(TO)$ and E_2^2 mode is phase shifted by 90°, being maximal when $E_1(TO)$ is minimal and vice versa. In order to thoroughly investigate such angle-dependent vibration behavior and determine the Raman tensor of the A_1, E_1, and E_2 modes in wurtzite AlN, theoretical simulations and analyses of Raman selection rules are necessary, which will be carried out in the next section.

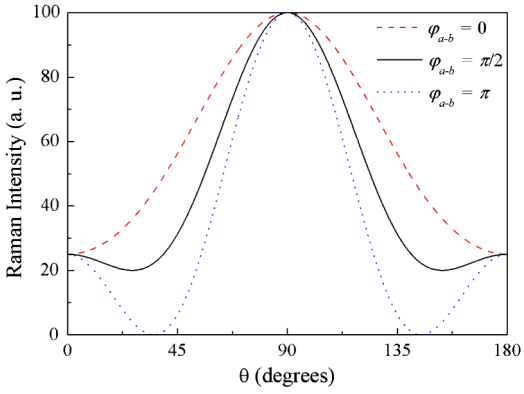

Fig. 2. Simulated Raman intensity according to Eq. (7) for an A_1 phonon measured on the *m*-plane surface of a crystal with wurtzite-type structure. θ is the rotated angle between the z axis of the sample and the polarization vector of incident light. The values of the parameters $|a|$ and $|b|$ for all curves are assumed as 5 and 10, respectively, and the value of phase difference φ_{a-b} varies from 0 (top curve) to π(bottom curve) with a step of $\pi/2$.

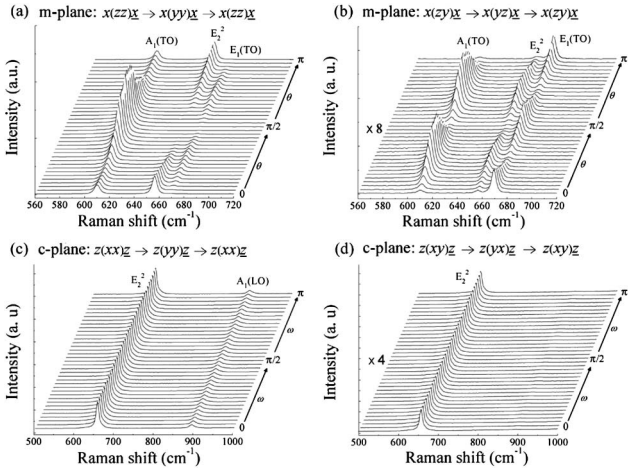

Fig. 3. (a) and (b) show the Raman spectra from the *m*-plane surface of the AlN sample for different rotation angles, shifted by a constant amount on the x and y axes, for parallel $[x(zz)\underline{x} \rightarrow x(yy)\underline{x} \rightarrow x(zz)\underline{x}]$ and perpendicular $[x(zy)\underline{x} \rightarrow x(yz)\underline{x} \rightarrow x(zy)\underline{x}]$ polarization vectors of the incoming laser and the scattered light, respectively. (c) and (d) record the angle-dependent Raman spectra from the *c*-plane of the AlN sample for parallel $[z(xx)\underline{z} \rightarrow z(yy)\underline{z} \rightarrow z(xx)\underline{z}]$ and perpendicular $[z(xy)\underline{z} \rightarrow z(yx)\underline{z} \rightarrow z(xy)\underline{z}]$ polarization vectors, respectively. For clarity, the ordinates in (b) and (d) have been magnified eight and four times, respectively, compared to those in (c) and (d).

Angle-dependent Raman spectra from the *c*-plane surface of the AlN sample in the range of 500–1000 cm^{-1} for parallel and perpendicular polarization vectors of the incoming laser and the scattered light are shown in Figs. 3(c) and 3(d), respectively. In Fig. 3(c), two allowed modes with FWHM less

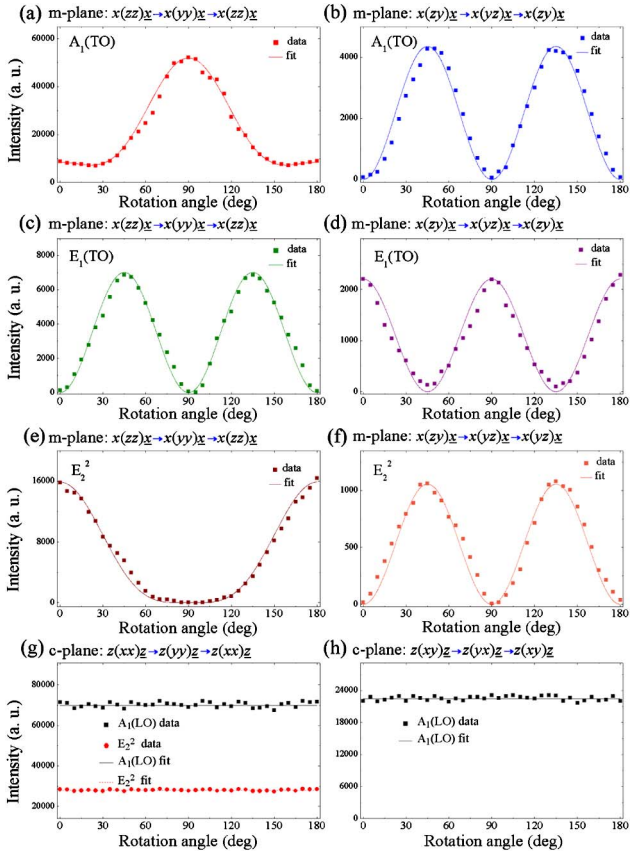

Fig. 4. (a) and (b) show the angle-dependent intensity of the $A_1(TO)$ signal from the *m*-plane surface of the AlN sample for parallel and perpendicular polarization vectors of incoming laser and the scattered light, respectively. The solid lines fit for determination of parameters $|a|$ and $|b|$ and φ_{a-b} based on Eqs. (10) and (14). (c) and (d) show the intensity of the $E_1(TO)$ signal from the *m*-plane surface versus the rotation angle for parallel and perpendicular polarization vectors, respectively, while (e) and (f) present the intensity of the E_2^2 signal versus the rotation angle for different polarizations. (a) and (b) record the angle-independent intensity of $A_1(LO)$ and E_2^2 signals from the *c*-plane surface of the AlN sample for parallel and perpendicular polarization versus the rotation angle ω.

than 3.8 cm^{-1} located at around 657, and 891 cm^{-1}, which are constant angle dependent, are ascribed to phonon modes E_2^2 and $A_1(LO)$, respectively. The constant angle dependence of two such allowed phonon modes is in agreement with the calculated selection rules as Eqs. (13) and (15). The low intensity of the $A_1(LO)$ signal observable in Fig. 3(c), according to Callender *et al.*, is due to suppression caused by destructive interference of the deformation potential with the Fröhlich contributions [30]. The constant angle-dependent vibration behavior of such Raman spectra scattering from the *c*-plane surface shown in Figs. 3(c) and 3(d) is obviously different from that scattering from the *m*-plane surface shown in Figs. 3(a) and 3(b), which is attributed to the isotropic arrangement of atoms in the *c*-plane. In Fig. 3(d), only the E_2^2 mode with FWHM less than 3.8 cm^{-1} located at around 657 cm^{-1} is allowed and is in agreement with the calculated selection rules as Eqs. (16)–(18). In addition, it is worth noting that the $E_1(LO)$ phonon mode does not appear in Figs. 3(c) and 3(d), because this phonon mode is forbidden in the backscattering geometry here. Sander *et al.* suggested that a weak signal of the $E_1(LO)$ mode would occur when the measured geometry deviates from an ideal backscattering geometry [26]. The unallowed $E_1(LO)$ mode reveals that deviations of our measured backscattering geometry are negligible.

B. Raman Tensor of AlN

The Raman intensities of the $A_1(TO)$, $E_1(TO)$, E_2^2, and $A_1(LO)$ phonon modes for parallel and perpendicular polarization geometries, as shown in Figs. 3(a)–3(d), are extracted from Lorentzian fitting. The fitting results, which are plotted versus the rotation angle for the two polarization geometries, are shown in Figs. 4(a)–4(h) as squares. The error bars of fitting results are too small to be clearly illustrated in the figures. To determine the Raman tensor elements, the angle variations are fitted with the functions calculated in Section 3 using least-squares fit procedures. The best fitting curves shown in Fig. 4 are in agreement with experimental data. The ratios of the fit parameters yield the relative values of the Raman tensor elements for AlN, which are summarized in Table 1. As a comparison, the relative values of the Raman tensor elements for ZnO crystal are also listed in Table 1, and are taken from Ref. [26].

AlN and ZnO, both of which are advanced wide-band-gap semiconductor compounds, can be potentially applied in the optoelectronic field, and they have the same wurtzite symmetry that belongs to the space group C_{6v}^4 ($P6_3mc$). During Raman scattering, six modes ($2A_1 + 2E_1 + 2E_2$) for wurtzite AlN and ZnO are active. Among these modes, the A_1 branch is polar mode polarized in the *z* direction. In doped semiconductors, the A_1 branch can influence the electronic transport properties due to the resonant coupling of polar phonons and plasmons (free carrier systems) [31]. As shown in Table 1, the ratio of $|a|/|d|$ for the $A_1(LO)$ phonon of AlN is much smaller than that for $A_1(TO)$, which is mainly attributed to $A_1(LO)$ suppression caused by destructive interference of the deformation potential with the Fröhlich contributions [30]. Such a small ratio of $|a|/|d|$ for $A_1(LO)$ is also observed in ZnO as shown in Table 1. Therefore, it is believed that the Raman tensor elements of $|a|$ and $|b|$ extracted from the $A_1(TO)$ mode are more accurate.

For $A_1(TO)$ of AlN, the amplitude of $|a|$ is about twice as strong as that of $|d|$. However, this is different from the situation of ZnO whose amplitude of $|a|$ is about half that of $|d|$. Determination of the ratio of $|a|/|d|$ is necessary since it reflects the Raman tensor anisotropy of the polar A_1 mode. The $|a|/|b|$ ratio of AlN is up to 2.5, while that of ZnO is only 1.0. The large $|a|/|b|$ ratio of AlN leads to an intensity ratio $I^{xx}_{A_1(TO)}/I^{yy}_{A_1(TO)}$ [e.g., $I(90°)/I(0°)$ of Fig. 4(a)] of more than 6.5, as we reported previously [32], while the $I^{xx}_{A_1(TO)}/I^{yy}_{A_1(TO)}$ of ZnO is only 1.1 [26], where the superscripts represent the polarization vector of incoming and scattering light. Such results reveal that the Raman tensor of the A_1 mode in AlN has strong anisotropy, which could be caused by its large difference in bond polarity.

As shown in Table 1, the phase difference φ_{a-b} between elements $|a|$ and $|b|$ of AlN is 91.24° and 91.18° for parallel and cross-polarized scattering geometries. The phase difference φ_{a-b} of AlN is still close to that of ZnO, despite the fact that the anisotropy ratios of $|a|/|b|$ for AlN and ZnO differ by a factor of about 1.5. This implies that the origin of the anisotropy ratio should differ from that of the phase difference for the A_1 Raman tensor elements in a wurtzite crystal.

Table 1. Relative Values of the Raman Tensor Elements of A_1, E_1, and E_2 Modes in Wurtzite AlN are Extracted from the Theoretical Fits to Angle-Dependent Raman Spectra for Parallel and Perpendicular Polarization Vectors of the Incoming Laser (e_i) and the Scattered Light (e_s)[a]

Raman Tensor Elements			$e_i \| e_s$		$e_i \perp e_s$	
			AlN	ZnO (Ref. [26])	AlN	ZnO (Ref. [26])
m-plane	A_1(TO)	$\|a/d\|$	1.818 ± 0.011	0.611 ± 0.006	1.846 ± 0.005	0.585 ± 0.022
	A_1(TO)	$\|b/d\|$	0.730 ± 0.008	0.599 ± 0.005	0.746 ± 0.004	0.413 ± 0.039
	A_1(TO)	φ_{a-b}	91.24°	93.00°	91.18°	104.00°
	E_1(TO)	$\|c/d\|$	0.671 ± 0.007	0.424 ± 0.004	0.721 ± 0.003	0.404 ± 0.001
	E_2^2	$\|d/d\|$	1.000 ± 0.009	1.000 ± 0.002	1.000 ± 0.004	1.000 ± 0.004
c-plane	A_1(LO)	$\|a/d\|$	0.408 ± 0.004	0.121 ± 0.001		
	E_2^2	$\|d/d\|$	1.000 ± 0.008	1.000 ± 0.002		

[a]Raman tensor elements for all phonon modes are normalized to that of the E_2 mode.

While this problem is not addressed here, it would be interesting to repeat the present Raman scattering measurement on other materials with wurtzite structure to determine the relationship between the anisotropy ratio and the phase difference.

Figures 4(a) and 4(b) show the angle-independent intensity of A_1(LO) and E_2^2 phonon modes, recording from the *c*-plane surface of the AlN sample for parallel and crossed polarization vectors of the incoming laser and the scattered light, respectively. The relative values of the Raman tensor elements for the *c*-plane AlN can be extracted by dividing the square root of the mean values of the fitted areas, which are also summarized in Table 1.

The second-rank Raman tensor $\boldsymbol{R}$ describes the characteristics of a phonon with respect to Raman scattering, which is an entity proportional to the Raman susceptibility [28]

$$\frac{\partial \boldsymbol{\chi}}{\partial \zeta} = V_c^{1/2} \sum_i^{\text{unit-cell}} \frac{\partial \boldsymbol{\chi}}{\partial u_i} M_i^{-1/2} \mathbf{e}_i, \tag{19}$$

where $\boldsymbol{\chi}$ denotes the polarizability tensor (the dipole moment induced by an unit incident electric field), ξ denotes the normal mode coordinate, V_c denotes the volume of the primitive cell, u_i and M_i represent the static atomic displacement and the mass of atom i, and $\mathbf{e}_i$ is the eigenvector of the vibrational mode. In this work, we determined the Raman tensor of AlN using angle-dependent polarized Raman spectra. In addition, the Raman tenor can also be calculated by Eq. (19). However, such a first-principles calculation is too difficult to achieve. A semi-empirical method based on the concept of bond polarizabilities, which only depends on the band length l of two neighboring ions, has been developed to estimate $\partial\boldsymbol{\chi}/\partial u_i$ and successfully used to interpret the Raman spectra in semiconductors [33]. It is well known that the wurtzite-type polar crystals, such as AlN, GaN, and ZnO, have two polar bonds (in-plane bond and out-plane band) with different lengths [34]. We believe that the unique Raman scattering behaviors of AlN bulk single crystal are related to its bond polarizabilities.

5. CONCLUSION

The angle-dependent Raman spectra for the *m*-plane and *c*-plane surfaces of an AlN single crystal for parallel and crossed polarized scattering geometries at room temperature were presented and discussed. The variations of intensity for A_1(TO), E_1(TO), A_1(LO), and E_2 modes versus rotation angle were calculated according to the Raman selection rules. The Raman tensor elements of such modes were determined by a combination of the experiment data and the calculated results. Moreover, the Raman tensor elements for A_1(TO), E_1(TO), A_1(LO), and E_2 of AlN were compared with that of ZnO, and the differences of the Raman tensor between AlN and ZnO were demonstrated.

ACKNOWLEDGMENTS

This work was financially supported by the Special Program for the State Key Program of National Natural Science of China (No. 61136001) and the Major Research Plan of the National Natural Science Foundation of China (No. 91333207).

REFERENCES

1. Y. Taniyasu, M. Kasu, and T. Makimoto, "An aluminium nitride light-emitting diode with a wavelength of 210 nanometres," Nature **441**, 325–328 (2006).
2. T. Oto, R. G. Banal, K. Kataoka, M. Funato, and Y. Kawakami, "100 mW deep-ultraviolet emission from aluminium-nitride-based quantum wells pumped by an electron beam," Nat. Photonics **4**, 767–770 (2010).
3. A. BenMoussa, J. F. Hochedez, R. Dahal, J. Li, J. Y. Lin, H. X. Jiang, A. Soltani, J.-C. De Jaeger, U. Kroth, and M. Richter, "Characterization of AlN metal-semiconductor-metal diodes in the spectral range of 44–360 nm: photoemission assessments," Appl. Phys. Lett. **92**, 022108 (2008).
4. S. J. Zinkle, V. A. Skuratov, and D. T. Hoelzer, "On the conflicting roles of ionizing radiation in ceramics," Nucl. Instrum. Methods Phys. Res. B **191**, 758–766 (2002).
5. G. Yu, *Properties of Advanced Semiconductor Materials GaN, AlN, InN, BN, SiC, SiGe* (Wiley, 2001).
6. I. Ahmad, V. Kasisomayajula, M. Holtz, J. M. Berg, S. R. Kurtz, C. P. Tigges, A. A. Allerman, and A. G. Baca, "Self-heating study of an AlGaN/GaN-based heterostructure field-effect transistor using ultraviolet micro-Raman scattering," Appl. Phys. Lett. **86**, 173503 (2005).
7. M. Kuball, S. Rajasingam, A. Sarua, M. J. Uren, T. Martin, B. T. Hughes, K. P. Hilton, and R. S. Balmer, "Measurement of temperature distribution in multifinger AlGaN/GaN heterostructure field-effect transistors using micro-Raman spectroscopy," Appl. Phys. Lett. **82**, 124–126 (2003).
8. A. J. Kent and J. K. Wigmore, *Electron-Phonon Interactions in Low-Dimensional Structures* (Oxford University, 2003).
9. O. Brafman, G. Lengycl, S. S. Mitra, P. J. Gielisse, J. N. Plendl, and L. C. Mansur, "Raman spectra of aluminum nitride, cubic boron nitride and boron phosphide," Solid State Commun. **6**, 523–526 (1968).
10. J. A. Sanjurjo, E. López-Cruz, P. Vogl, and M. Cardona, "Dependence on volume of the phonon frequencies and their effective charges of several III-V semiconductors," Phys. Rev. B **28**, 4579–4584 (1983).

11. M. Kuball, J. M. Hayes, A. D. Prins, N. W. Van Uden, D. J. Dunstan, Y. Shi, and J. H. Edgar, "Raman scattering studies on single-crystalline bulk AlN under high pressures," Appl. Phys. Lett. **78**, 724–726 (2001).
12. C. Carlonc, K. M. Lakin, and H. R. Shanks, "Optical phonons of aluminum nitride," J. Appl. Phys. **55**, 4010–4014 (1984).
13. L. McNeil, M. Grimsditch, and R. H. French, "Vibrational spectroscopy of aluminum nitride," J. Am. Ceram. Soc. **76**, 1132–1136 (1993).
14. M. Kuball, J. M. Hayes, Y. Shi, and J. H. Edgar, "Phonon lifetimes in bulk AlN and their temperature dependence,"Appl. Phys. Lett. **77**, 1958–1960 (2000).
15. J. M. Hayes, M. Kuball, Y. Shi, and J. H. Edgar, "Temperature dependence of the phonons of bulk AlN," Jpn. J. Appl. Phys. **39**, L710 (2000).
16. D. Y. Song, M. Holtz, A. Chandolu, S. A. Nikishin, E. N. Mokhov, Y. Makarov, and H. Helava, "Optical phonon decay in bulk aluminum nitride," Appl. Phys. Lett. **89**, 021901 (2006).
17. P. Pandit, D. Y. Song, and M. Holtz, "Decay of zone-center phonons in AlN with A_1, E_1, and E_2 symmetries," J. Appl. Phys. **102**, 113510 (2007).
18. L. Bergman, M. Dutta, C. Balkas, R. F. Davis, J. A. Christman, D. Alexson, and R. J. Nemanich, "Raman analysis of the E_1 and A_1 quasi-longitudinal optical and quasi-transverse optical modes in wurtzite AlN," J. Appl. Phys. **85**, 3535–3539 (1999).
19. H.-C. Hsu, G.-M. Hsu, Y.-s. Lai, Z. C. Feng, S.-Y. Tseng, A. Lundskog, U. Forsberg, E. Janzén, K.-H. Chen, and L.-C. Chen, "Polarized and diameter-dependent Raman scattering from individual aluminum nitride nanowires: the antenna and cavity effects," Appl. Phys. Lett. **101**, 121902 (2012).
20. F. Bernardini, V. Fiorentini, and D. Vanderbilt, "Spontaneous polarization and piezoelectric constants of III-V nitrides," Phys. Rev. B **56**, R10024(R) (1997).
21. Y. Taniyasu, M. Kasu, and T. Makimoto, "Radiation and polarization properties of free-exciton emission from AlN (0001) surface," Appl. Phys. Lett. **90**, 261911 (2007).
22. R. G. Banal, M. Funato, and Y. Kawakami, "Optical anisotropy in [0001]-oriented $Al_xGa_{1-x}N$/AlN quantum wells ($x > 0.69$)," Phys. Rev. B **79**, 121308(R) (2009).
23. L. C. de Carvalho, A. Schleife, F. Fuchs, and F. Bechstedt, "Valence-band splittings in cubic and hexagonal AlN, GaN, and InN," Appl. Phys. Lett. **97**, 232101 (2010).
24. J. Li, K. B. Nam, M. L. Nakarmi, J. Y. Lin, H. K. Jiang, P. Carrier, and S.-H. Wei, "Band structure and fundamental optical transitions in wurtzite AlN," Appl. Phys. Lett. **83**, 5163–5165 (2003).
25. H. L. Wu, R. S. Zheng, Z. Yan, M. M. Li, and W. Zheng, "Effect of temperature distribution on growth habit of AlN crystal," J. Shenzhen Univ. Sci. Eng. **29**, 487–491 (2012).
26. T. Sander, S. Eisermann, B. K. Meyer, and P. J. Kar, "Raman tensor elements of wurtzite ZnO," Phys. Rev. B **85**, 165208 (2012).
27. T. Strach, J. Brunen, B. Lederle, J. Zegenhagen, and M. Cardona, "Determination of the phase difference between the Raman tensor elements of the A_{1g}-like phonons in $SmBa_2Cu_3O_{7-\delta}$," Phys. Rev. B **57**, 1292–1297 (1998).
28. M. Cardona and G. Guntherodt, *Light Scattering in Solid II* (Springer, 1982), pp. 22–45.
29. R. Loudon, "The Raman effect in crystals," Adv. Phys. **13**, 423–482 (1964).
30. R. H. Callender, S. S. Sussman, M. Selders, and R. K. Chang, "Dispersion of Raman cross section in CdS and ZnO over a wide energy range," Phys. Rev. B **7**, 3788–3798 (1973).
31. D. Olego and M. Cardona, "Raman scattering by coupled LO-phonon-plasmon modes and forbidden TO-phonon Raman scattering in heavily doped p-type GaAs," Phys. Rev. B **24**, 7217–7232 (1981).
32. W. Zheng, R. S. Zheng, H. L. Wu, and F. D. Li, "Strongly anisotropic behavior of A_1(TO) phonon mode in bulk AlN," J. Alloys Compd. **584**, 374–376 (2014).
33. S. Go, H. Bilz, and M. Cardona, "Bond charge, bond polarizability, and phonon spectra in semiconductors," Phys. Rev. Lett. **34**, 580–583 (1975).
34. W. Zheng, Z. C. Feng, J. Lee, D. Wuu, and R. S. Zheng, "Lattice deformation of wurtzite $Mg_xZn_{1-x}O$ alloys: an extended X-ray absorption fine structure study," J. Alloys Compd. **582**, 157–160 (2014).